

# Instability and unsteadiness of aircraft wake vortices

L. Jacquin<sup>a,\*</sup>, D. Fabre<sup>b</sup>, D. Sipp<sup>a</sup>, V. Theofilis<sup>c</sup>, H. Vollmers<sup>d</sup>

<sup>a</sup> *Department of Fundamental and Experimental Aerodynamics, ONERA, 8 rue des Vertugadins, 92190 Meudon, France*

<sup>b</sup> *IMFT, allée du professeur Camille Soula, 31400 Toulouse, France*

<sup>c</sup> *Escuela Técnica Superior Ingenieros Aeronáuticos, Universidad Politécnica de Madrid, plaza cardenal Cisneros 3, E 28040 Madrid, Spain*

<sup>d</sup> *Institute of Aerodynamics and Flow Technology, DLR, Bunsenstrasse 10, D-37073 Göttingen, Germany*

Received 17 October 2001; received in revised form 8 April 2003; accepted 2 June 2003

## Abstract

This paper presents a review of theoretical and experimental results on stability and other unsteady properties of aircraft wakes. The basic mechanisms responsible for the propagation and the amplification of perturbation along vortices, namely the Kelvin waves and the cooperative instabilities, are first detailed. These two generic unsteady mechanisms are described by considering asymptotic linear stability analysis of model flows such as vortex filaments or Lamb–Oseen vortices. Extension of the linear analysis to more representative flows, using a biglobal stability approach, is also described. Experimental results obtained using LDV, hot wire and PIV in wind tunnels are presented and they are commented upon the light of theory.

© 2003 Published by Elsevier SAS.

*Keywords:* Aircraft wake; Vortex dynamics; Stability theory; Nonparallel global stability theory; Unsteady flow; Turbulence; Laser velocimetry; Hot wire velocimetry; Particle image velocimetry

## 1. Introduction

Two strategies may be considered to produce less harmful wakes behind aircraft, see e.g. [19,24]. The first is to increase the characteristic radii of the final vortices so as to decrease the rolling momentum of a following aircraft during encounters. This effect may be achieved by introducing “as much turbulence as possible” into the vortex system. The second strategy is to promote the development of cooperative instabilities occurring in a system of several vortices, which leads to destructive interactions between the two halves of the wake. Theoretical analysis and specific measurements are both needed to investigate this topic.

As it will be shown, useful theoretical results are provided by linear stability analysis of generic flows. Linear instability theory enables the introduction of important physical mechanisms which lead to unsteadiness. As for the experiments, wind tunnel tests give access to measurements within downstream distances limited to typically ten model

spans. In this regime, the wake unsteadiness is dominated by small amplitude displacements of the vortex cores. Due to the presence of very sharp velocity gradients within the cores, this “meandering” of the vortices leads to the observation of large amplitude velocity fluctuations in both LDV and hot wire measurements. PIV-measurements also show the fluctuation of tip and flap edge vortices. Examples will be described in Section 4. These wind tunnel tests can be prolonged by using a catapult facility, as described in [7].

The paper is organised as follows. Section 2 describes the average properties of a vortex wake, considering at first a simple wake model, and then a wind tunnel experiment. In Section 3 a review of basic linear mechanisms occurring in vortex wakes is presented, with a particular emphasis on the Kelvin waves and the cooperative instabilities. The review also presents the kinds of methods that may be used to study these mechanisms, such as vortex filament methods, asymptotic methods, and biglobal instability analysis methods. In Section 4 some experimental observations of the unsteady properties of a vortex wake are presented, and are discussed in the light of theory. Conclusions and perspectives are listed in Section 5.

\* Corresponding author.

*E-mail address:* [laurent.jacquín@onera.fr](mailto:laurent.jacquín@onera.fr) (L. Jacquin).

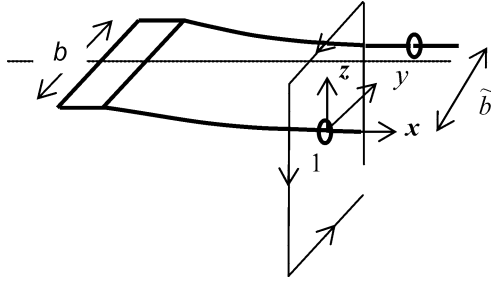


Fig. 1. Sketch of the far-field wake downstream of a wing.

## 2. Average properties of a typical vortex wake

### 2.1. A simple model

In this section we first consider a simplified wake model composed of a single vortex pair. This approach allows us to introduce the main properties and length-scales of a vortex wake and to relate these features to the properties of the generating wing. The configuration is sketched in Fig. 1. The wing is characterised by its lift coefficient  $C_L$ , span  $b$ , surface  $S$  and aspect ratio  $AR = b^2/S$ . The mean flow velocity is noted  $V_\infty$ . The vorticity  $\omega$  is directed in the axial ( $x$ ) direction, and is antisymmetrical with respect to the symmetry plane  $y = 0$ .

The main measure of the intensity of the wake is the circulation, computed in a half-plane of the wake

$$\Gamma = \int_{-\infty}^0 \int_{-\infty}^{\infty} \omega \, dy \, dz. \quad (1)$$

A characteristic length-scale of the wake can then be defined as the effective span  $\tilde{b}$

$$\tilde{b} = \frac{1}{\Gamma} \int_{-\infty}^{\infty} \int_{-\infty}^{\infty} y \omega \, dz \, dy. \quad (2)$$

In case of a single vortex pair,  $\Gamma$  and  $\tilde{b}$  obviously correspond to the circulation of the vortices and their separation. Moreover, these measures are still relevant in the case where the wake is composed of a larger number of vortices, since  $\tilde{b}$  then corresponds to the distance between vorticity centroids. In the case of an elliptic loading, the effective span is related to the wing span through  $\tilde{b} = (\pi/4)b$ . Now, from conservation of vertical momentum, the lift,  $1/2 C_L \rho V_\infty^2 S$ , is equal to the flux of vertical momentum of the wake,  $\rho V_\infty \Gamma \tilde{b}$ . The circulation is therefore given by  $\Gamma = 2 C_L V_\infty b / \pi AR$ . For a landing transport aircraft one typically has  $C_L \approx 1.5$ ,  $AR \approx 7$ .

In order to characterise the internal structure of the vortices, several vortex core length-scales may be defined (see [24]). A common definition is the “dispersion radius”, corresponding to

$$\bar{r}^2 = \frac{1}{\Gamma} \int_{-\infty}^{\infty} dz \int_0^{+\infty} dy \{((y - y_c)^2 + (z - z_c)^2) \omega\}, \quad (3)$$

where  $y_c$  and  $z_c$  are the coordinates of the vorticity centroid in half a plane. This length-scale provides an evaluation of the vorticity field dispersion. Other integral definitions of the vortex core have been proposed, and their properties are discussed by Jacquin et al. [24]. However, as will be shown below, specification of a single measure of the vortex core hardly reflects the actual structure of the vortices.

### 2.2. An experimental illustration

We now illustrate the properties of a realistic vortex wake with some results taken from the wind tunnel experiment of Jacquin et al. [24]. In this experiment the wake of a generic A300 model was investigated by means of laser Doppler velocimetry (LDV). The model had a wing span  $b = 448$  mm and was set in two configurations, a cruise configuration (noted “clean case”) and a high lift configuration (noted

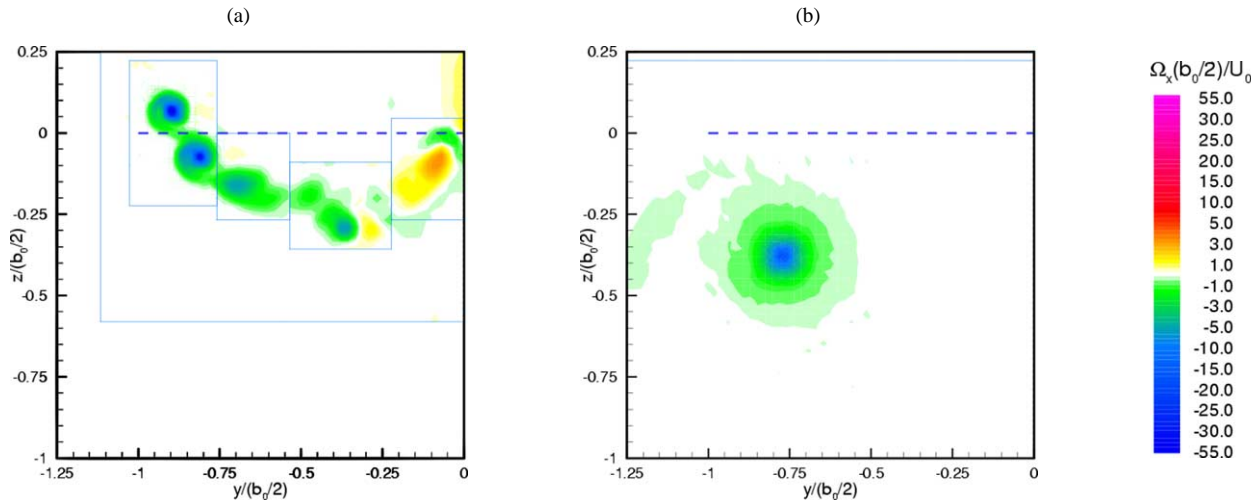


Fig. 2. Axial vorticity measured by LDV in the left-hand side of the wake of the A300 model of Jacquin et al. [24] in high-lift configuration, for downstream distances  $X/b = 0.5$  (a) and  $X/b = 9$  (b).

“high lift”), with wings fitted with single block flaps. The lift coefficients were respectively  $C_L \approx 0.7$  and  $1.7$ . Tests have been performed for a free-stream velocity  $V_\infty = 50 \text{ ms}^{-1}$ . The Reynolds number based on the aerodynamic chord  $c \approx 66 \text{ mm}$  was  $Re_c \approx 220000$ . Fig. 2 displays the axial vorticity in the left-hand side of the wake for the high-lift configuration, measured at two downstream distances  $X$  corresponding respectively to  $X/b = 0.5$  (a) and  $X/b = 9$  (b). At the first position (Fig. 2(a)), the wake consists of a vortex sheet which rolls up into several vortices. In addition to the wing tip vortices, secondary vortices are formed at the discontinuities of the wing: the flap edges, the nacelle and the wing-fuselage junction. Note the existence of a counter-rotating vortex in the inner parts of the wake, close to the position of the inner edge of the flap. At downstream distance  $X/b = 9$  (Fig. 2(b)), it is observed that all the vortices have merged into a single vortex in each half-plane. Things are similar for the clean configuration, except that a smaller number of vortices are obtained due to the absence of flaps.

The structure of the vortices after completion of the roll-up and merging phases was investigated in detail. Fig. 3

shows the tangential velocity  $V_\theta$  after cylindrical averaging of the LDV measurements at a downstream distance of 5 wing spans behind the model for both configurations. This figure reveals that at least two core length-scales are required to give an accurate description of a realistic vortex. One may thus define an “internal core” (or “viscous core”) of radius  $r_1$ , rotating as a solid body, and an “external core” (or “inviscid core”) of radius  $r_2$ , which characterises the region containing vorticity surrounding the internal core (see [43]). In both configurations, the internal core is found to be extremely narrow. The maximum velocity is reached for an internal radius  $r_1$  which is less than 1% of the span  $b$ . In an intermediate zone surrounding the internal core, the velocity law then follows a power law of the form  $r^{-\alpha}$  with  $\alpha$  close to 0.5. This power law representation is particularly clear in the logarithmic plot 3(b), which indicates the exact value of the slopes for both configurations. Such a power law is in accordance with the classical model proposed by Betz [2], which leads to  $\alpha = 0.5$  for a wing with an elliptic load, and with the self-similar roll-up solution of Kaden (see [39]). In both configurations departure from these laws occurs at an external core radius close to  $r_2/b \approx 0, 1$ . Away from this external core the velocity law grossly decays as  $r^{-1}$ . Note that for the high lift configuration, a ‘plateau’ region, with a velocity almost constant, is also observed between the internal core and the power law region. Such a velocity plateau was also observed by Devenport et al. [6]; as suggested by these authors, this could correspond to a remnant of the initial conditions due to a merging of several cores. In the present experiment, the merging between the wing tip and the flap tip vortices occurs close to  $x/b = 2$ .

A two scale model of the type

$$\begin{aligned} r \leq r_1: V_\theta &= Ar, \\ r_1 \leq r \leq r_2: V_\theta &= Br^{-\alpha}, \\ r \geq r_2: V_\theta &= \Gamma/2\pi r \end{aligned} \tag{4}$$

has been proposed to model the flow (the constants  $A$  and  $B$  are defined so as to ensure the continuity of the velocity field). This model is sketched in Fig. 4. The choice  $\alpha \approx 0.5$ ,  $r_1/b \approx 0.01$ ,  $r_2/b \approx 0.1$  is suggested by the experiment presented above, and is also consistent with other experiments [43].

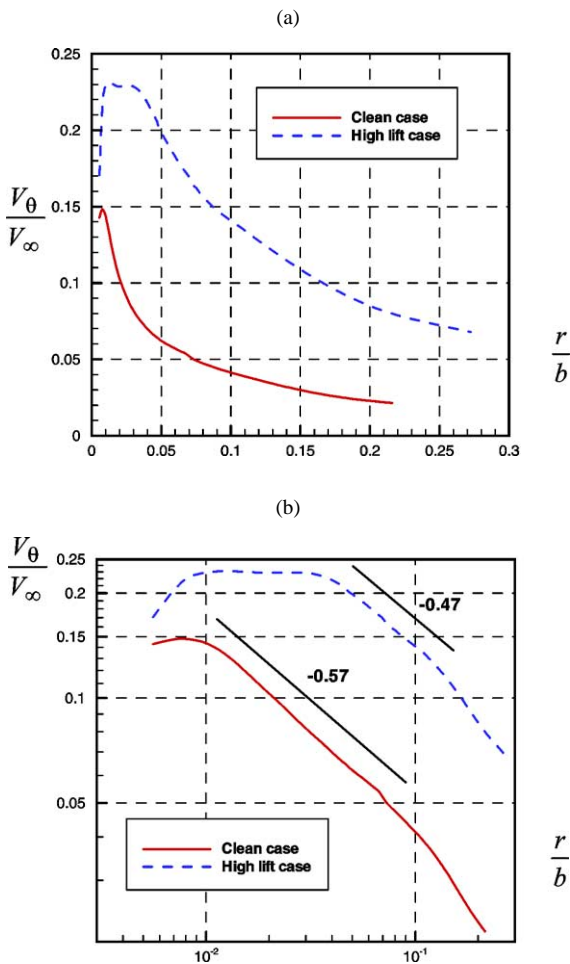


Fig. 3. Tangential velocity law  $V_\theta/V_\infty$  as function of the radial distance from the vortex center, for the A300 model in clean and high-lift configurations. (a) lin-lin plot, (b) log-log plot (from [24]).

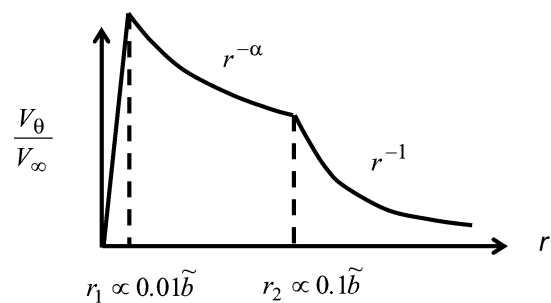


Fig. 4. The two core scales vortex model.

### 3. Linear dynamics of wake vortices

This section presents a review on basic linear mechanisms. We successively present the Kelvin waves (Section 3.1), the long-wave (Section 3.2) and short-wave (Section 3.3) cooperative instabilities, the instabilities due to core axial flow (Section 3.4), as well as the specific method used to describe them. We then describe a more general stability approach based on the biglobal method (Section 3.5).

#### 3.1. Kelvin waves

Any perturbation in a rotating flow leads to the propagation of dispersive waves, called inertia waves. These waves are equivalent to gravity waves in a stably stratified medium. The inertia waves propagating along a vortex are named Kelvin waves. The case of a basic flow corresponding to a Rankine vortex (with constant vorticity core) has been extensively described in the literature (see e.g. [38,39]). Here we consider the case of a Lamb–Oseen vortex with circulation  $\Gamma$  and radius  $a$ . The angular velocity is given by

$$\Omega(r) = \frac{V_\theta(r)}{r} = \frac{\Gamma}{2\pi r^2} (1 - e^{-r^2/a^2}). \quad (5)$$

We restrict the study to the inviscid case which has been described by Sipp [40], Sipp and Jacquin [42]. This study was recently extended to account for the effect of viscosity by Fabre [12], Fabre, Sipp and Jacquin [18]. Interestingly, it was shown that only axisymmetric ( $m = 0$ ) and helical ( $m = 1$ ) modes are significant, and that modes with azimuthal wave-numbers  $|m| \geq 2$  are much more damped. Consequently we restrict here to the  $m = 0$  and  $m = 1$  cases. More realistic models, such as the two scale model introduced above, were also considered by Fabre [12]. Results do not differ much from the Lamb–Oseen case.

##### 3.1.1. Method

In the inviscid case the Kelvin waves are described by solving an eigenvalue problem resulting from the linearization of the Euler equations around the basic flow specified above. We introduce the following small perturbations

$$(v'_x, v'_r, v'_\theta, p') = (F, iG, H, P)(r)e^{i(kx+m\theta-\omega t)} \quad (6)$$

where  $v'_x, v'_r, v'_\theta$  are the axial, radial and azimuthal components of the velocity and  $p'$  the pressure.  $\omega = \omega_r + i\omega_i$  denotes a complex frequency. Following Howard and Gupta [23], Lessen, Singh and Paillet [31], we are led to the following second order equation for the variable  $Z = rG(r)/\gamma(r)$

$$Z'' - AZ' - BZ = 0 \quad (7)$$

with

$$A = \frac{1}{r} - \frac{2m\Omega'}{\gamma} - \frac{2k^2r}{m^2 + k^2r^2},$$

$$B = k^2 + \frac{m^2}{r^2} - \frac{2m\Omega'}{\gamma r} - \frac{4mk^2\Omega}{\gamma(m^2 + k^2r^2)} - \frac{2k^2\Omega\mathcal{E}}{\gamma^2},$$

where  $\mathcal{E}(r) = 1/r(d(rV_\theta)/dr)$  is the basic flow axial vorticity and  $\gamma(r) = m\Omega(r) - \omega$ . With the boundary conditions  $Z(0) = Z(\infty) = 0$ , this equation constitutes an eigenvalue problem for  $\omega$ . This problem admits a countable infinity of eigenvalues indexed as  $\omega_{m,n}(k)$  where  $k$  and  $m$  are the axial and azimuthal wave-numbers and where the absolute value of second index  $|n|$  is related to the number of zeros of the eigen-function (the higher the label, the more radial oscillations the mode contains). The sign of  $n$  is used to distinguish different families of waves. Resolution is achieved using a shooting method. Results are shown in Fig. 5 for the axisymmetric modes  $m = 0$  and the helical modes  $m = 1$ . The frequencies are made nondimensional with the rotation rate of the vortex center, given by  $\Omega_0 = \Gamma/2\pi a^2$ .

##### 3.1.2. Axisymmetric modes ( $m = 0$ )

For axisymmetric modes ( $m = 0$ ), see Fig. 5(a), the results are very similar to those obtained with a Rankine vortex. The waves form two families of branches which propagate in opposite directions. Note that the group velocity  $d\omega_r/dk$ , which corresponds to the slope of the differ-

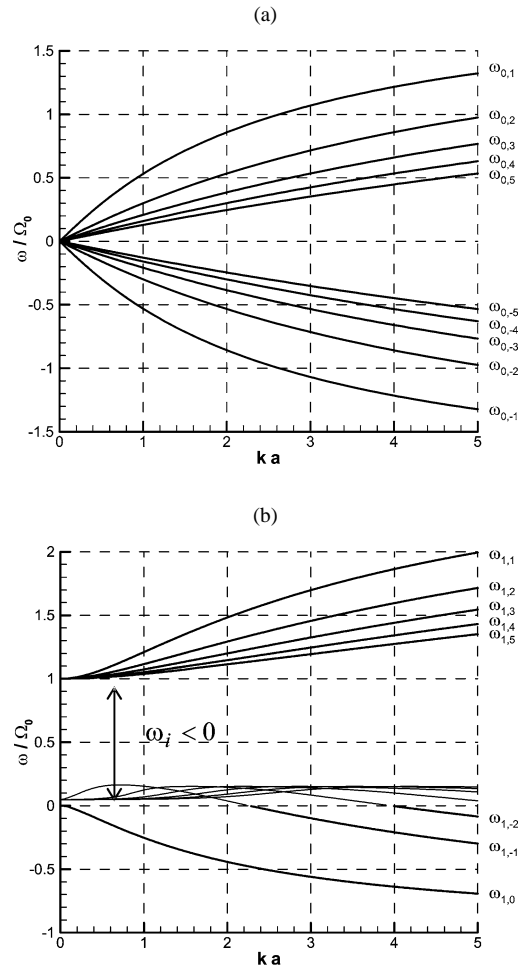


Fig. 5. Frequencies  $\omega_r$  of the Kelvin waves in a Lamb–Oseen vortex: (a) axisymmetric modes  $m = 0$ , (b) helical modes  $m = 1$ .  $\Omega_0 = \Gamma/2\pi a^2$  (from [15]).

ent branches, decreases with the wave-number. The fastest waves are found on the branch  $\omega_{0,1}$  in the limit of long wavelength ( $ka \rightarrow 0$ ). The group velocity of this wave is found to be

$$\frac{d\omega_{0,1}(k)}{dk} \approx 0.63 \frac{\Gamma}{2\pi a}. \quad (8)$$

Interestingly, in a Lamb–Oseen vortex, one finds that the maximum tangential velocity is  $V_{\theta \max} \approx 0.63\Gamma/(2\pi a)$ . This result means that the energy of axisymmetric perturbations propagates with a speed smaller than the maximum tangential velocity of the vortex:

$$\frac{d\omega_{0,n}(k)}{dk} \leq V_{\theta \max}.$$

This property also holds for more realistic vortex models [12]. In the case where  $V_{\theta \max}/V_{\infty} < 1$ , which holds in trailing vortices, energy of the perturbations is convected downstream, and the flow is thus supercritical. This property prevents the possibility of perturbation energy travelling upstream at a higher speed than that of the flow, a necessary condition for occurrence of a “hydraulic jump” leading to vortex breakdown.

### 3.1.3. Helical modes ( $m = 1$ )

Due to the symmetries of the base flow, one has  $\omega_{1,n} = -\omega_{-1,n}$ . Accordingly, the helical waves must be considered by pairs, the left-handed modes ( $m = 1$ ) propagating along the vortex core in opposite directions than their right-handed counterparts ( $m = -1$ ). We restrict to the case of left-handed modes. Some differences are observed with respect to the case of a Rankine vortex, in particular for the modes which possess a critical layer. Such modes occur whenever the angular phase speed of the perturbation,  $\omega_r/m$ , coincides with the angular velocity of the vortex  $\Omega(r_c)$  at some radius  $r_c$ , i.e.  $\text{Re}\{\gamma(r_c)\} = 0$ . For  $m = 1$  this condition occurs in the range  $0 < \omega_r < \Omega_0$ . The corresponding modes are singular, and have to be regularised by the introduction of viscosity (see [12]). A careful analysis shows that these modes are necessarily damped, i.e.  $\omega_i < 0$  (a necessary condition for this is that the mean flow vorticity  $\mathcal{E}(r_c)$  at the critical radius be nonzero, and this condition is always fulfilled for a Lamb–Oseen vortex). Outside this interval, the modes are regular and purely oscillatory. According to their angular frequency  $\omega_r/m$ , these regular modes can be classified into co-rotating waves ( $\omega_r/m > \Omega_0$ ) and counter-rotating waves ( $\omega_r/m < 0$ ).

Fig. 5(b) displays the real frequencies  $\omega_r$  of the helical modes, with thin lines for the singular damped modes and thick lines for the regular modes. It is found that helical modes are of three different kinds, which are now successively described.

– The branch labeled  $\omega_{1,0}$  corresponds to the wave with the simplest structure (eigenfunction with no zeroes). This wave is counter-rotating, and is called the “slow wave” because both the frequency and the phase velocity  $c = \omega_r/k$  (and also the group velocity  $d\omega_r/dk$ ) tend towards

zero when  $k$  goes to zero. This mode takes the form of a helical displacement of the vortex core as a whole, and it actually corresponds to the self-induced oscillation mode of a filament vortex (see [39]). The frequency of this mode in the limit of long wavelength ( $ka \ll 1$ ) has been obtained using asymptotic methods by Moore and Saffman [34] and Leibovich et al. [29]:

$$\omega_{\pm 1,0}/\Omega_0 \approx \mp \frac{k^2 a^2}{2} \left( \ln \left( \frac{2}{ka} \right) - 0.6358 \right). \quad (9)$$

This mode plays an important role in the linear dynamics of a vortex; in particular, it is involved in the long-wave cooperative instabilities that will be considered in Section 3.2. Consequently, it might be interesting to have a uniform approximation of this frequency valid for all  $k$ . Fabre [12] proposed the following expression

$$\omega_{\pm 1,0} \equiv \frac{\mp (ka)^2 \Omega_0}{2 + C_1 |ka| + C_2 (ka)^2} \left( \ln \left( \frac{2 + C_3 |ka|}{|ka|} \right) + C_4 \right). \quad (10)$$

The choice  $C_1 = 3.19407$ ,  $C_2 = 1.46081$ ,  $C_3 = 8.13352$ ,  $C_4 = -0.63518$ , which has been determined using a least-square method, gives an accurate fit of the solution actually computed by the eigenvalue method for a Lamb–Oseen vortex. Alternatively, the choice  $C_1 = 0.95508$ ,  $C_2 = 0.43848$ ,  $C_3 = 2.15048$ ,  $C_4 = -0.32722$  can be used for a Rankine vortex.

– The branches labelled  $\omega_{1,n}$ ,  $n = 1, 2, \dots$ , correspond to co-rotating waves. The long-wave asymptotic behaviour of these branches has been given by Leibovich et al. [29]

$$\omega_{1,n}/\Omega_0 \approx 1 + \frac{2(ka)^2}{(1+n)(2+n)}. \quad (11)$$

These waves are sometimes referred to as “fast waves” because their phase velocity tends to  $\infty$  as  $k \rightarrow 0$ . However, according to (11), the group velocity of these “fast waves” tends to zero with  $k$ . Calculation of their spatial structure shows that in the limit  $k \rightarrow \infty$ , these modes become concentrated in a very small region near the vortex axis and that, consequently, they are strongly affected by viscosity, see [12].

– The branches labelled  $\omega_{1,-n}$ , with  $n = 1, 2, \dots$  are either counter-rotating neutral waves, or damped critical layer waves. The transition occurs at particular wave-numbers where  $\omega_r = 0$ , corresponding to steady Kelvin waves. For a Lamb–Oseen vortex, see Fig. 5(b), these wave-numbers are found to be  $ka \approx 2.26, 3.96, 5.61, \dots$ . The superposition of these  $m = 1$  waves with their  $m = -1$  counterparts leads to steady untwisted perturbations. The vorticity field associated with such a perturbation (for  $ka = 2.26$ ) is shown in Fig. 6. Such steady untwisted perturbations are particularly interesting because they can be destabilised by the straining field imposed by other vortices. This mechanism is responsible for the Widnall instability, which will be considered in detail in Section 3.3.

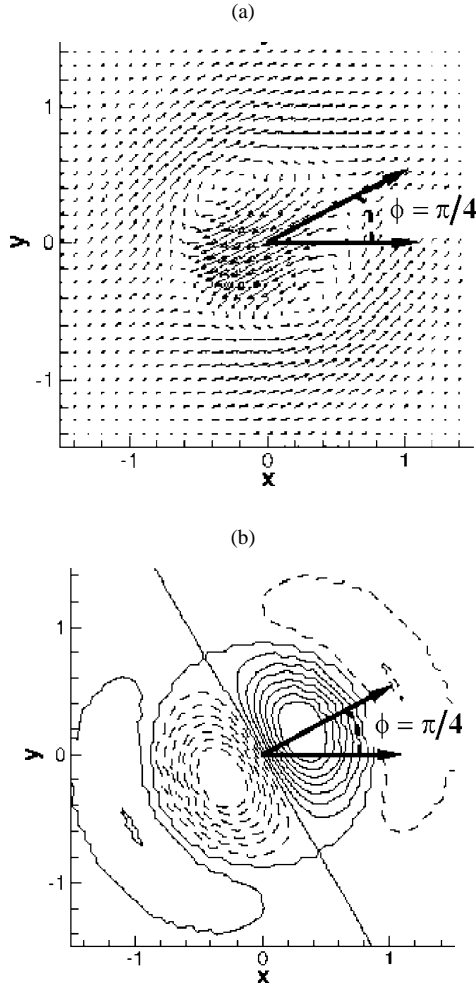


Fig. 6. Vorticity of the perturbation produced by the superposition of two opposite Kelvin waves  $m = 1$  and  $m = -1$  on a Lamb–Oseen vortex. (a) Vorticity in the plane orthogonal to the vortex axis, (b) axial vorticity (from [41]).

### 3.2. Long-wave cooperative instabilities

#### 3.2.1. Method

As shown in Section 2.2, the wake issuing from a high lift designed wing is usually composed of several vortex filaments. In general, such a vortex arrangement is unstable with respect to 3D perturbations due to mutual straining of the vortices.

Following [4,5,15], a system of stability equations may be derived by considering a set of parallel vortex filaments with slight sinusoidal perturbations of their respective positions. We suppose that the centerline position  $(Y_n(t), Z_n(t))$  of the vortex filament labelled  $n$  is displaced with an amplitude proportional to  $e^{ikx}$  where  $x$  is the coordinate in the axial direction

$$\underline{X}_n(x, t) = x \underline{e}_x + (Y_n(t) + \hat{y}_n(t)e^{ikx}) \underline{e}_y + (Z_n(t) + \hat{z}_n(t)e^{ikx}) \underline{e}_z. \quad (12)$$

At the leading order, linearisation of the Biot–Savart law leads to the system

$$\begin{aligned} \frac{dY_n}{dt} &= \sum_{m \neq n} -\frac{\Gamma_m}{2\pi} \frac{Z_n - Z_m}{R_{mn}^2}, \\ \frac{dZ_n}{dt} &= \sum_{m \neq n} \frac{\Gamma_m}{2\pi} \frac{Y_n - Y_m}{R_{mn}^2}, \end{aligned} \quad (13)$$

where  $R_{mn}^2 = (Y_m - Y_n)^2 + (Z_m - Z_n)^2$ . This system describes the evolution of a set of  $N$  point vortices. At the following order, the equations which describe the evolution of the perturbation amplitude vector  $\underline{X}(t) = (\hat{y}_1, \hat{z}_1, \dots, \hat{y}_N, \hat{z}_N)$  may be written in the following form

$$\frac{d\underline{X}(t)}{dt} = \underline{L}(t) \underline{X}(t). \quad (14)$$

The developed expressions of this linear system are given by Crow [4] and Jimenez [26] for the cases of counter rotating and corotating vortex pairs, respectively, and by Crouch [5] and Fabre, Jacquin and Loof [15] in the general case. The right hand side of (14) amounts to the superposition of three effects: (i) the straining experienced by filament  $n$  when displaced from its mean position in the velocity field induced by an undisturbed filament  $m$ , (ii) the self induced rotation of the disturbed filament  $n$  and (iii) the velocity field induced on the filament  $n$  by the other vortices when they are sinusoidally displaced from their mean positions.

Mechanism (i) may be easily understood when considering the 2D flow corresponding to a pair of straight counter-rotating vortex filaments separated by a distance  $h = \tilde{b}$ , as in Fig. 1. In a coordinate system moving downward with a speed  $dZ/dt = -\Gamma/(2\pi\tilde{b})$ , linearization of (13) around the centre of the vortex labelled 2, i.e.  $r/\tilde{b} \ll 1$  with  $r^2 = (y - Y_2)^2 + (z - Z_2)^2$ , leads to

$$\begin{pmatrix} dy/dt \\ dz/dt \end{pmatrix} = \frac{\Gamma}{2\pi\tilde{b}^2} \begin{pmatrix} 0 & 1 \\ 1 & 0 \end{pmatrix} \begin{pmatrix} y \\ z \end{pmatrix}. \quad (15)$$

This velocity field is that of a strain with rate  $\Gamma/(2\pi\tilde{b}^2)$  whose axes are oriented at  $\pm 45^\circ$  with respect to the horizontal ( $x$ ) axis. It leads to amplification of any perturbation of the vortex centerline, the latter being displaced away when it leaves its initial position.

The self induced rotation terms, mechanism (ii), reads

$$\begin{pmatrix} d\hat{y}_n/dt \\ d\hat{z}_n/dt \end{pmatrix} = \frac{\Gamma_n}{2\pi a_n^2} \varpi(k a_n) \begin{pmatrix} 0 & 1 \\ -1 & 0 \end{pmatrix} \begin{pmatrix} \hat{y}_n \\ \hat{z}_n \end{pmatrix} \quad (16)$$

which introduces a dependence of the solution with respect to a measure  $a_n$  of the vortex core radius. This dependence describes a self-induced rotation of the perturbed vortex in an opposite direction to that of the basic state. This effect results from the velocity that a curved vortex filament induces on itself. Several methods have been used to compute the frequency  $\varpi$  of this self-induced oscillation. Crow [4] initially used the Biot–Savart law with a cutoff method. Widnall et al. [52] and Moore and Saffman [34] then identified this oscillation mode with the slow Kelvin

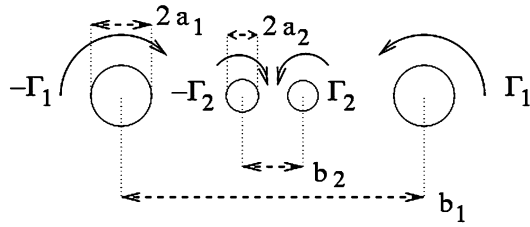


Fig. 7. Four-vortex wake model.

wave described in Section 3.1, and evaluated its frequency with the asymptotic expression given in Eq. (9) with the positive sign. This method is valid in the long-wave limit  $ka \ll 1$ , and it leads to the prediction of spurious short-wave instabilities outside its range of validity. A better method is to use the uniform expression (10) given above (again with the positive sign) instead of the asymptotic one. If the vortices are not Rankine or Lamb–Oseen ones, the constants  $C_1, C_2, C_3, C_4$  may of course be adjusted to fit with the actual frequency computed with an eigenvalue method. Alternatively, as suggested in [15], the result for a Rankine vortex may be used in all cases provided that the core radius  $a_n$  is defined as the *effective core radius* of the vortex (see [13,15] for further details).

3.2.2. Example: stability of four-vortex configurations

Let us consider the example of two vortex pairs, as sketched in Fig. 7. The vortex pairs may be co-rotating ( $\Gamma_1 > 0, \Gamma_2 > 0$ ) or counter-rotating ( $\Gamma_1 > 0, \Gamma_2 < 0$ ). The first case may model wing tip vortices and flap tip vortices whereas the second one could model merged wing and flap tip vortices and merged inner flap and horizontal tail vortices. The stability of these configurations can be studied using the vortex filament method presented above provided that the core radii of the vortices are small with respect to their separations, i.e.

$$a_1, a_2 \ll b_1, b_2, (b_1 - b_2)/2. \tag{17}$$

The system (13) which describes the evolution of the mean position of the vortices may be integrated analytically. Depending upon the circulation ratio  $\Gamma_2/\Gamma_1$  and the separation ratio  $b_2/b_1$ , the system may be periodic (the vortices orbit around their vorticity centroids in each half plane), divergent (the inner and outer vortex pairs separate), or stationary (the vortices remain aligned and descend at a constant speed). Fig. 8 shows a classification chart of these configurations, initially displayed by Donaldson and Bilanin [8]. Stationary configurations are found on the curve of equation

$$\left(\frac{b_2}{b_1}\right)^3 + 3\frac{\Gamma_2}{\Gamma_1}\left(\frac{b_2}{b_1}\right)^2 + 3\frac{b_2}{b_1} + \frac{\Gamma_2}{\Gamma_1} = 0. \tag{18}$$

This condition was also derived by Rennich and Lele [37].

The stability of the four-vortex configuration was first considered by Crouch [5] in the case of co-rotating vortex pairs ( $\Gamma_1 > 0, \Gamma_2 > 0$ ) using a Floquet analysis. Fabre and Jacquin [14] then considered the stationary configurations

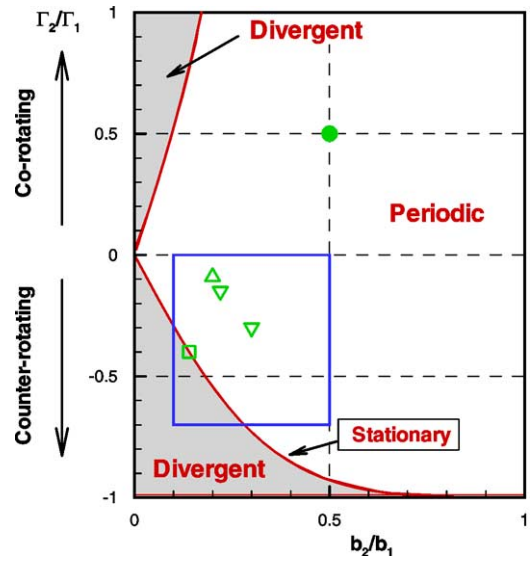


Fig. 8. Classification chart of the four-vortex configurations. ● [5], □ [14], ▲▼: ONERA experiments, rectangular box: [15].

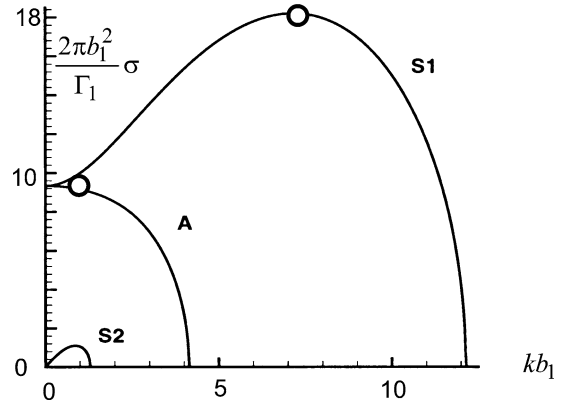


Fig. 9. Growth rate of unstable eigenmodes as function of the axial wave number for the four-vortex stationary configuration with  $\Gamma_2/\Gamma_1 = -0.4, b_2/b_1 = 0.14, a_1/b_1 = 0.1, a_2/b_1 = 0.05$ .  $S_1, S_2$ : symmetric modes, A: antisymmetric modes. Mode  $S_2$  is the Crow instability mode (from [14]).

using an eigenvalue method. This study was then extended to periodic or divergent counter-rotating configurations, see Fig. 8, by Fabre, Jacquin and Loof [15] using an optimal perturbation analysis. Let's consider first the results obtained by Fabre and Jacquin [14] for the stationary configuration with  $\Gamma_2/\Gamma_1 = -0.4, b_2/b_1 = 0.14, a_1/b_1 = 0.1, a_2/b_1 = 0.05$ , a case which was also considered by Rennich and Lele [37] by means of numerical simulation. Fig. 9 sketches the amplification rate  $\sigma$  of the unstable eigenmodes. Three unstable branches are obtained. Two of them correspond to symmetrical modes (noted  $S_1, S_2$ ), and the third one to an antisymmetrical mode (noted A). In the two-dimensional case ( $k = 0$ ), both  $S_1$  and A modes are unstable, with an amplification rate close to  $\sigma \approx 9\Gamma_1/(2\pi b_1^2)$ . The maximum of amplification is reached on the branch  $S_1$  for short wavelengths ( $kb_1 \approx 7$ ). The branch, labelled  $S_2$  is limited to long wavelengths ( $kb_1 < 1.2$ ). It is close to the classical Crow instability that would develop on the outer vortices

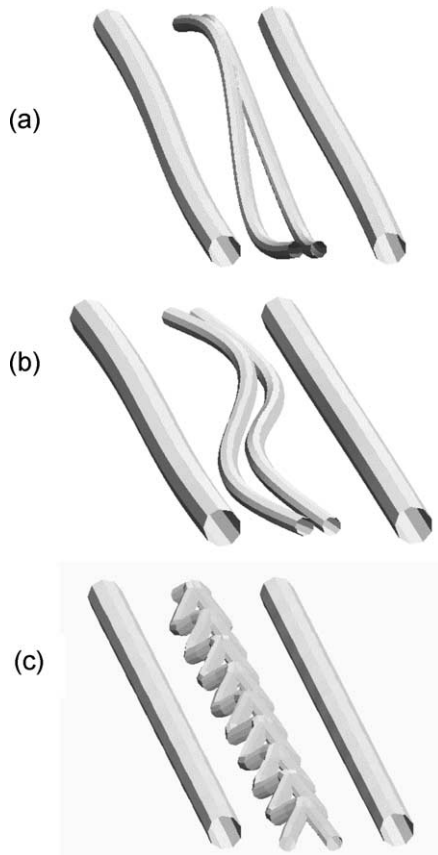


Fig. 10. Instability in a stationary four vortex configuration: (a) Long-wave symmetric (S1) mode, (b) long-wave antisymmetric (A) mode, (c) short-wave symmetric (S1) mode. These modes are identified by circles in Fig. 9 (from [14]).

if they were isolated, with a wavelength  $kb_1 \approx 0.8$  and an amplification rate  $\sigma_{\text{Crow}} \approx 0.8\Gamma_1/(2\pi b_1^2)$  (see [4]).

The shape of the symmetric and antisymmetric modes corresponding to  $kb_1 \approx 0.8$  are sketched in Fig. 10(a)–(b). The most amplified mode is that sketched in Fig. 10(c). This mode appears to be essentially a Crow instability acting on the inner vortices. This mode leads to a rapid linkage of these inner vortices and has almost no effect on the outer ones. A practical conclusion of this work was that the naturally emerging mode, obtained without forcing of a long wavelength mode, will be a short wavelength instability localised on the inner vortices that will not affect the outer vortices.

As shown by Fabre, Jacquin and Loof [15], similar conclusions hold for unsteady configurations. An example is shown in Fig. 11 which corresponds to the most amplified (optimal) perturbation which develops in a four vortex system such that  $\Gamma_2/\Gamma_1 = -0.3$ ,  $b_2/b_1 = 0.3$ . Considering that the vortices of Fig. 7 are emitted by a wing of span  $b_0$ , of lift coefficient  $C_L = 1.5$  and aspect ratio  $AR = 7$  (which are typical of an aircraft in landing configuration), the temporal evolution of the perturbation may be translated into downstream distances (see [15] for further details). The optimal growth  $G^{\text{opt}}$  is defined as the ratio between the final and initial amplitudes of the optimal perturbation.

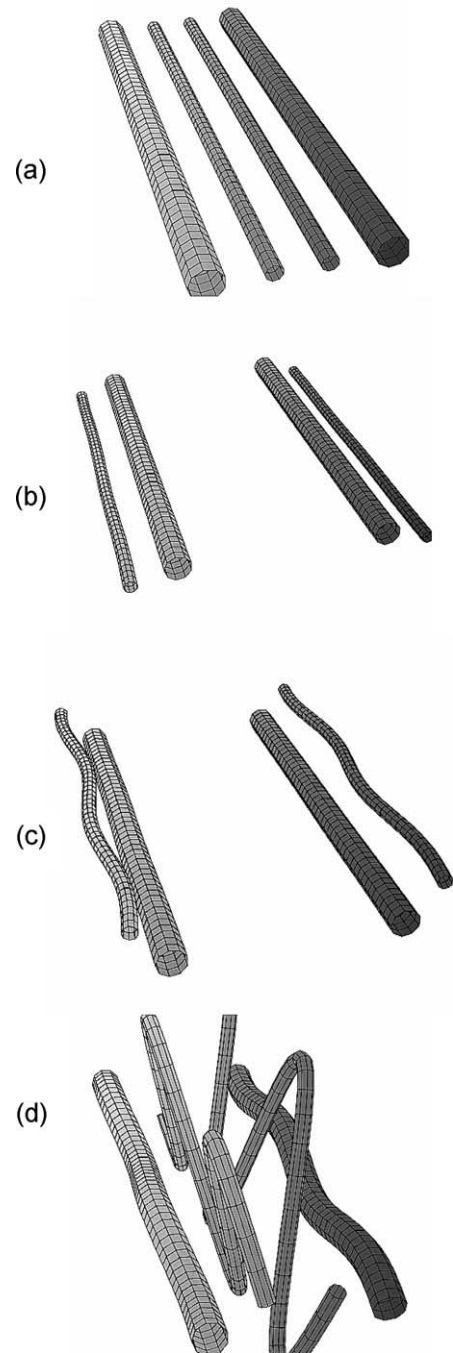


Fig. 11. Optimal perturbation in a periodic four vortex configuration with  $\Gamma_2/\Gamma_1 = -0.3$ ,  $b_2/b_1 = 0.3$ : (a)  $X/b_0 = 0$ , (b)  $X/b_0 = 10$ , (c)  $X/b_0 = 20$ , (d)  $X/b_0 = 30$ . The vortices are emitted by a wing of span  $b_0$ , of lift coefficient  $C_L = 1.5$ , aspect ratio  $AR = 7$  [15].

In the case of Fig. 11, at  $X/b_0 = 30$  the optimal growth is  $G^{\text{opt}} = 5677$ . As a comparison, for a single vortex pair with equivalent conditions, the growth rate of the Crow [4] instability is 2.2, and for the corotating four-vortex configuration considered by Crouch [5] the growth rate is close to 10. The wave-number of the perturbation is  $k^{\text{opt}}b_1 = 4.55$  which gives a wavelength  $\lambda^{\text{opt}}/b_1 \approx 1.38$ , a value smaller than that of the Crow instability. Note that this perturbation is antisymmetrical. This type of perturbation

has been observed in towing tank experiments, see [36]. Two-point LDV measurements performed by Jacquin et al. [24] behind a representative aircraft also suggest that such a four-vortex interaction could participate to the global unsteadiness of the vortices in the extended near-wake field.

These examples demonstrate that introduction of counter-rotating vorticity in the wake of an aircraft contributes to destabilise the wake. However, the non-linear evolution of the system after the collapse of the vortices (downstream  $X/b_0 = 30$ , considering Fig. 11) remains unknown.

### 3.3. Short-wave cooperative instabilities

#### 3.3.1. Method

As mentioned above, the individual vortices of the wake are subjected to a straining field imposed by the presence of the other vortices. Such a straining field has been described in (15) for a counter-rotating vortex pair; it corresponds to a strain of rate  $\Gamma/(2\pi\tilde{b}^2)$  with axes oriented  $\pm 45^\circ$  which is responsible for the displacement of the two vortex filaments in the Crow instability mechanism.

Now, considering the flow within the core, the strain field amplifies, by stretching, any vorticity perturbations aligned with the strain axis, such as that in Fig. 6(a). This mechanism, called Widnall instability, may be quantified by means of a multiple time scale analysis, see [35,50]. Considering the flow evolution on the characteristic length and time scales  $L = a$  and  $T = 2\pi a^2/\Gamma$ , the strain amounts to a perturbation at order  $\varepsilon = (a/\tilde{b})^2$ . The assumption

$$\varepsilon = \left(\frac{a}{\tilde{b}}\right)^2 \ll 1 \quad (19)$$

allows an asymptotic approach. Using polar co-ordinates, the strain field depends on the second harmonic  $\exp(2i\theta)$ . The total divergence-free basic velocity field in the plane normal to the vortex axis may then be expressed into the form

$$\underline{U} = \underline{U}_0(r) + \varepsilon \underline{U}_1(r, \theta) + \dots \quad (20)$$

with

$$\underline{U}_0(r) = (0, r\Omega(r), 0)^t,$$

$$\underline{U}_1(r) = (f \sin 2\theta/R, f' \cos 2\theta/(2r), 0)^t.$$

The stream-function at order  $\varepsilon$  is  $\psi_1(r, \theta) = -f(r) \cos 2\theta/2$ . The function  $f(r)$  must be determined so that (20) fulfils the steady Euler equations at order  $\varepsilon$ , see [35]. Considering 3D perturbations, i.e. two Kelvin waves with azimuthal wave-number  $m_1$  and  $m_2$ , with an amplitude of the order  $\delta \ll 1$ , a resonance occurs at the order is, presumably,  $\delta\varepsilon$ . The mechanism described with this method is a global resonant interaction between three steady perturbations, i.e. two Kelvin waves and the strain, which takes place as soon as the triadic resonance relation  $m_1 - m_2 = 2$  is satisfied. For the Lamb–Oseen vortex, it only occurs for  $m_1 = 1, m_2 = -1$ . In the Rankine vortex other

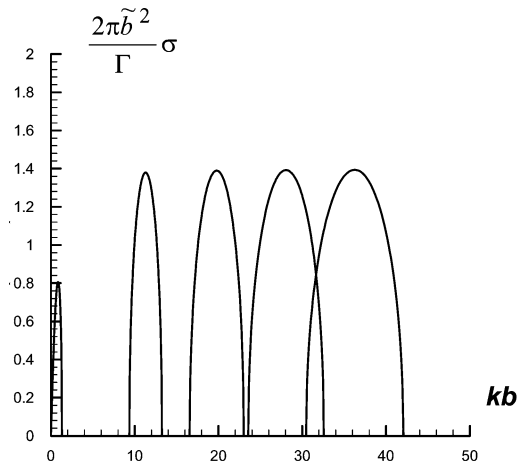


Fig. 12. Amplification rate of the short-wave co-operative instabilities in a pair of Lamb–Oseen vortices with  $a/\tilde{b} = 0.2$ .

Kelvin modes may be involved, such as  $m_1 = 2, m_2 = 0$  (see [9,35]).

The amplification rate  $\sigma = \omega_i$  of these cooperative instabilities, as obtained using Moore and Saffman's method described above, reads

$$\sigma = (\Gamma/2\pi\tilde{b}^2) \sqrt{R^2 - [\varepsilon(ka - k_c a)Q]^2}. \quad (21)$$

This rate corresponds to a narrow band of instability of width  $|ka - k_c a| < \varepsilon R/Q$  where  $k_c$  is the wave number such that  $\omega_{\pm 1, n}(k_c) = 0$ . The peak of instability is reached for  $ka = k_c a$  in which case  $\sigma = R\Gamma/2\pi\tilde{b}^2$ . The constant  $Q$  and  $R$  have to be determined as functions of the actual vortex model. The Rankine vortex was considered by Tsai and Widnall [50] and Eloy and Le Dizes [11]; the Lamb–Oseen vortex was treated by Eloy and Le Dizes [10] and Sipp and Jacquin [42], and the two core scales vortex model given by equation (4) was investigated by Fabre and Jacquin [16].

As an example, Fig. 12 shows the amplification rate of the instabilities due to resonance of the straining field with the helical waves ( $\omega_r = 0, m = \pm 1, ka \approx 2.26, 3.96, 5.61 \dots$ ) for a Lamb–Oseen dipole of aspect ratio  $a/\tilde{b} = 0.2$ . The results are plotted here versus  $k\tilde{b}$ . The first lobe, close to the origin  $k\tilde{b} = 0$ , corresponds to the Crow instability. The short-wave instabilities concern wave numbers  $k\tilde{b} \geq 9$ .

#### 3.3.2. Results and discussion

The status about the cooperative instabilities is the following:

- The amplification rate of these short wave cooperative instabilities in Lamb–Oseen vortices is  $\sigma = 1.4\Gamma/(2\pi\tilde{b}^2)$ , see Fig. 12. It is slightly larger than the amplification rate of the Crow instability,  $\sigma_{\text{Crow}} \approx 0.8\Gamma/(2\pi\tilde{b}^2)$ . The time scales  $\tau$  of the two instabilities are thus equivalent and of the order  $O(2\pi\tilde{b}^2/\Gamma)$ .

- Compared with the viscous time scale  $\tau_v \propto a^2/\nu$ , we have  $\tau_v/\tau \propto (a/\tilde{b})^2 \text{Re}$ . Therefore, if we assume that  $a/\tilde{b} = O(0.1)$ , for  $\text{Re} \gg 100$ , the cooperative instabilities are free from viscous damping.

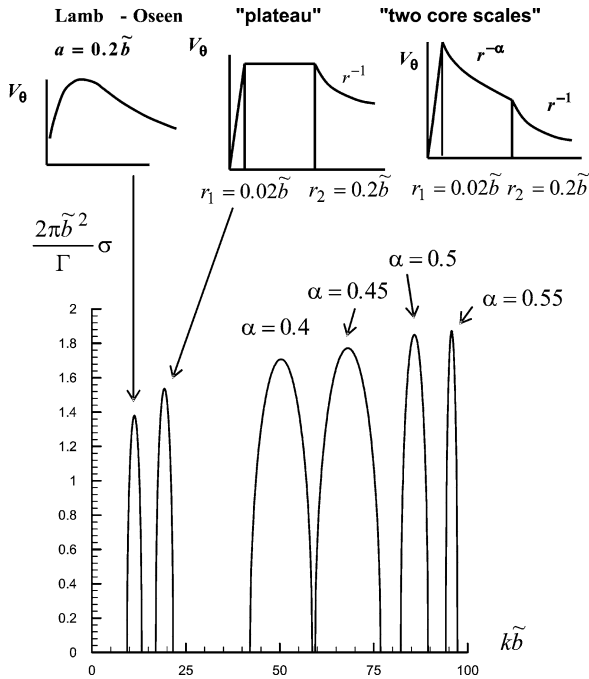


Fig. 13. Amplification rate of the first Widnall instability in pairs of vortices corresponding to different models: Lamb–Oseen ( $a/\tilde{b} = 0.2$ ), “plateau” and “two core scales”, with  $r_1/\tilde{b} = 0.02$ ,  $r_2/\tilde{b} = 0.2$ . For the two core scales model which is defined by Eq. (4), different values of the exponent  $\alpha$  have been considered.

– Dependence of cooperative instabilities on the vortex model is a question of importance. Only small differences are found when comparing two models based on a single scale, such as the Rankine vortex and the Lamb–Oseen vortex for instance: the most amplified wave numbers  $k_c$  and the amplification rates are comparable. The main difference is that in Lamb–Oseen vortices the presence of critical layers leads to the suppression of some resonances, such as the ones with  $m_1 = 0$ ,  $m_2 = 2$  (see [42]).

– Things become different when considering more representative models such as the one introduced in Fig. 4. Fig. 13 shows the first amplification lobes of the short wave instabilities obtained when considering three simplified vortex models. The first one is the Lamb–Oseen vortex pair, such that  $a/\tilde{b} = 0.2$ , the second one is a “plateau” vortex pair with a constant tangential velocity region from  $r_1/\tilde{b} = 0.02$  to  $r_2/\tilde{b} = 0.2$  and the third is a vortex pair corresponding to the model (4), with internal radius  $r_1/\tilde{b} = 0.02$ , external radius  $r_2/\tilde{b} = 0.2$  and several values of  $\alpha$ . In accordance with Fig. 12, the short-wave instabilities in the Lamb–Oseen dipole starts around  $k\tilde{b} \approx 12$ . Compared to this reference case, it is found that more realistic models lead to a shift towards smaller wavelengths of the instability lobes. The “plateau” model leads to occurrence of the first Widnall instability at a slightly higher wave-number ( $k\tilde{b} \approx 20$ ). In the case of two core scale vortices, the higher  $\alpha$ , the smaller are the unstable wavelengths. For instance, using  $\alpha = 0.5$ , it is found that the first short-wave cooperative instability is  $k_c\tilde{b} \approx 85$ . Introducing the radius  $r_1$ , one has  $k_c r_1 \approx 1.7$  which means that the instability scales with the inner core radius. Note that, inter-

estingly, the wavelength and the width of the instability band are extremely sensitive to the value of  $\alpha$  within the range of values observed in the experiments, see Section 2. This topic was recently explored by Fabre and Jacquin [16].

– An interesting theoretical result is that obtained by Sipp [41] using a weakly non-linear analysis of the Widnall instabilities of a strained Lamb–Oseen vortex. The result is that short-wave instabilities saturate very quickly. The mechanism responsible for this saturation is a sudden self-induced rotation of the plane waves that occurs when their amplitude becomes large. Detailed results show that the maximum vortex core distortion induced by the Widnall instability is then limited to values smaller than  $0.01\tilde{b}$  before non-linear interaction occurs, see [41].

In conclusion, the above results suggest that, in representative vortex wakes, the short-wave cooperative instabilities are likely confined in the very centre region of the vortex cores and that they cannot lead to significant core distortions before they saturate. Short-wave instabilities are unimportant as far as a counter-rotating vortex pair separated by a distance  $\tilde{b}$  is concerned, i.e. in the far-field wake. But things become different in the near-field where, as shown by Le Dizes and Laporte [28], the short-wave cooperative instabilities play an important role in the merging mechanism of co-rotating vortices.

### 3.4. Instabilities due to axial flow

To complete our review on basic linear mechanisms, we mention that another class of instabilities may develop in the presence of core axial flow in the vortices. These instabilities have been extensively studied for the model flow known as the  $q$ -vortex [1,33]. This model corresponds to a Gaussian jet superimposed to a Lamb–Oseen vortex, i.e.

$$U(r) = e^{-r^2}, \quad V_\theta(r) = q/r(1 - e^{-r^2}).$$

Three families of instabilities can be distinguished. The first ones are basically inviscid, and occur for  $q < 1.5$ . These instabilities are well described by the asymptotic study of Leibovich and Stewartson [30], which predicts that they take the form of ring-modes, with a structure concentrated in an annular region located around the core. Jacquin and Pantano [25] recently observed the development of these instabilities in a Direct Numerical Simulation of a  $q$ -vortex with an initial swirl number  $q = 1$ . They showed that the development of these instabilities initially leads to the development of a fine-scale turbulence. However due to the stabilising effect of rotation this turbulence is unable to survive, and the vortex progressively turns back to a laminar state with a swirl number larger than 1.5.

The second family of instabilities are the viscous modes evidenced by Khorrami [27]. These modes occur for  $q < 1.2$ , and their growth rates are several orders of magnitude smaller than those of the inviscid modes occurring in this range. Consequently, they are unlikely to play any role in the dynamics of vortex wakes.

Finally, the third family of instabilities are the viscous centre-modes recently described by Fabre and Jacquin [17]. These modes exist for very large Reynolds numbers, and for swirl number much larger than the other families of instabilities. So, they could be present in trailing vortices in the far wake. The significance of these kinds of instabilities in realistic aircraft wakes should be clarified by future numerical or experimental studies.

### 3.5. Biglobal instability analysis

The analysis of long- and short-wave perturbations conducted above can be merged using a more general approach, by relaxing the assumptions (17) and (19). Any flow quantity  $\underline{q} = (u, v, w, p)^T$  is again considered as

$$\underline{q}(x, y, z, t) = \underline{\bar{q}}(y, z) + \delta \underline{\tilde{q}}(x, y, z, t), \quad (22)$$

with a small-amplitude perturbation of order  $\delta$  and form

$$\underline{\tilde{q}}(x, y, z, t) = \underline{\hat{q}}(y, z)e^{i(kx - \omega t)} + \text{c.c.} \quad (23)$$

where  $\omega_r = \text{Re}\{\omega\}$  is related with the frequency of a biglobal eigenmode  $\underline{\hat{q}}$  while the imaginary part,  $\omega_i = \text{Im}\{\omega\}$  is its growth/damping rate. The objective of the analysis is still the identification of unstable eigenvalues  $\omega$  and associated eigen-vector amplitude functions  $\underline{\hat{q}}$  for a given basic state  $\underline{\bar{q}}$  describing the wake-vortex system. The system for the determination of  $\omega$  and the associated eigen-functions  $\underline{\hat{q}}$  in its most general form can be written as the complex nonsymmetric generalised eigenvalue problem [47]

$$\begin{cases} ik\hat{u} + D_y\hat{v} + D_z\hat{w} = 0, \\ L\hat{u} - (D_y\hat{u})\hat{v} - (D_z\hat{u})\hat{w} - ik\hat{p} = -i\omega\hat{u}, \\ [L - (D_y\hat{v})]\hat{v} - (D_z\hat{v})\hat{w} - D_y\hat{p} = -i\omega\hat{v}, \\ -(D_y\hat{w})\hat{v} + [L - (D_z\hat{w})]\hat{w} - D_z\hat{p} = -i\omega\hat{w}, \end{cases} \quad (24)$$

where the linear operator is

$$L = (1/\text{Re})(-k^2 + D_y^2 + D_z^2) - ik\hat{u} - \hat{v}D_y - \hat{w}D_z \quad (25)$$

and  $D_y = \partial/\partial y$ ,  $D_z = \partial/\partial z$ ,  $D_y^2 = \partial^2/\partial y^2$ ... Significant comments regarding the global instability analysis are, first, that the two-dimensional eigenvalue problem (24) permits considering wake-vortex systems having a velocity component  $\bar{u}$  in the direction of the aircraft motion,  $x$ , in addition to those defined on the  $Oyz$  plane,  $\bar{v}$  and  $\bar{w}$ ; the only assumptions of the analysis are

$$\partial \underline{\bar{q}}/\partial t = \partial \underline{\tilde{q}}/\partial x = 0 \quad (26)$$

the first of which may be relaxed in case of a time-periodic basic state by employing Floquet theory [3,22]. It should also be noted here that solution of one of the alternative simplified forms of the partial derivative eigenvalue problem (24) valid in the case of a single velocity component [44] or, additionally, in the inviscid limit [20], is not permissible in the wake-vortex stability problem.

Successful applications of biglobal instability analysis based on (24) are the studies of the swept attachment-line

boundary layer, Lin and Malik [32], who exploited the symmetries of that problem to reduce the computing effort, that of Theofilis [46,49] who solved (24) for the same configuration without resort to symmetries, as well as the analyses of Theofilis [45,48] in open and lid-driven cavity flows and that of Theofilis et al. [48] in boundary layer-flow which encompasses a closed recirculation bubble. Compared with the latter applications, in which a matrix eigenvalue problem of leading dimension in excess of  $10^4$  was solved using state-of-the-art numerical algorithms for the discretisation of (24) and efficient algorithms for the eigenspectrum, the wake-vortex system presents the additional challenge of yet higher resolution being necessary for the adequate description of the wake-vortex system basic flow itself and, consequently, the sought global instabilities.

One simplification which halves the storage requirements for the solution of (24) that are typically of the order of several gigabytes, is the case in which the basic flow velocity component  $\bar{u}$  is absent in the wake-vortex system. In conjunction of the definitions  $\tilde{\omega} = i\omega$ ,  $\tilde{w} = i\bar{w}$ , this simplification results in a *real* partial-derivative eigenvalue problem enabling storage of real arrays alone, as opposed to the complex arrays appearing in (24). Freeing half of the necessary storage results in the ability to address flow instability at substantially higher resolutions and/or higher Reynolds numbers compared with an analysis based on solution of (24). However, from a physical point of view, neglecting the axial velocity component  $\bar{u}$  in the basic flow restricts the classes of flows that can be addressed by a global instability analysis. With this consideration in mind, the potentiality of the method will be illustrated by considering the case of a system composed of Batchelor-like vortices, each of which is characterised by

$$\begin{aligned} \bar{u}(y, z) &= e^{-r^2}, \\ \bar{v}(y, z) &= q \cos \theta (1 - e^{-r^2})/r^2, \\ \bar{w}(y, z) &= q \sin \theta (1 - e^{-r^2})/r^2, \end{aligned} \quad (27)$$

where  $r = \sqrt{(y - y_n)^2 + (z - z_n)^2}/a_n$ ,  $(y_n, z_n)$  denotes the centre and  $a_n$  the radius of vortex  $n$ . Here the centreline axial velocity of the vortices has been taken equal to unity. In constructing a basic flow composed of several such vortices satisfying (27), the additional freedom exists in the choice of the relative circulation, radius and location of the vortices. The basic flow analysed here was constructed along the lines of those discussed in Section 3.2. It consists of two pairs of co-/counter-rotating vortices. A first case was constructed by taking  $q_1 = 1$  and  $q_2 = -0.5$  and assuming a stationary configuration fixed by the Rennich and Lele condition (18). The first vortex was placed at the outmost starboard location  $(x_1, y_1) = (7, 0)$ , lengths being made non-dimensional using the radius parameter of the outer vortices. The radii were chosen consistently with the definition (27),  $a_1 = 1$ ,  $a_2 = 0.5$ . The Rennich–Lele condition delivers the location of the second vortex  $(x_2, y_2) = (0, 1.27)$  in this case. The locations and swirl of these two vortices were

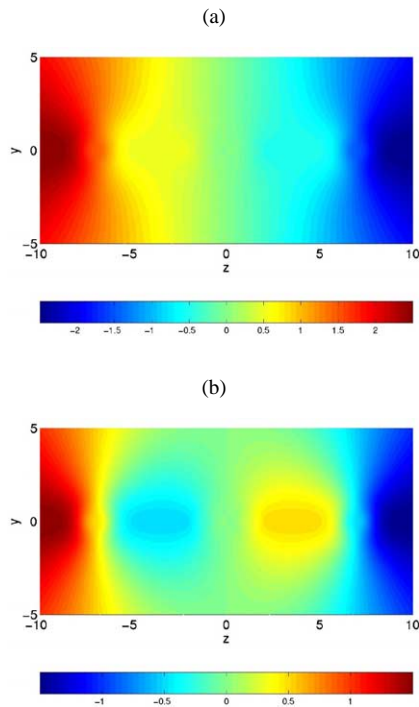


Fig. 14. Vertical velocity  $\bar{w}(y, z)$  of the basic flow considered: (a)  $q_2 > 0$  (co-rotating), (b)  $q_2 < 0$  (contra-rotating).

mirrored with respect to the centreline  $x = 0$  to construct the fields which are illustrated in Fig. 14(a) through the distribution of the vertical velocity  $\bar{w}(y, z)$ . A second case was constructed using the same vortex locations and  $q_1 = 1$ ,  $q_2 = 0.5$  (Fig. 14(b)). Such a configuration is not stationary.

A Reynolds number can be defined as  $Re_1 = q_1/v$ . The biglobal instability analysis was performed at  $Re_1 = 10^3$  and several axial periodicity wave-numbers  $k$ , of which results at a short wave number,  $k = 2/3$  i.e.  $L_x = 2\pi/k \approx 9.4$ , are indicated. Homogeneous Dirichlet boundary conditions have been imposed on all disturbance velocity components at the far-field and a compatibility condition was used on the disturbance pressure at the boundaries. A resolution analysis study was performed to ensure integrity of the results presented, using different grids,  $32^2$ ,  $56^2$  or  $64^2$  Legendre collocation points to resolve the two-dimensional domain considered,  $z \in [-10, 10] \times y \in [-5, 5]$ . Accordingly, the Krylov subspace dimension was increased from  $m = 200$  at the lowest- to  $m = 400$  at the highest-resolution runs. The resulting memory requirements for the recovery of the most interesting window of leading eigenvalues and eigenvectors at a single pair of the parameters  $(Re, k)$  ranged from 300 Mbytes to 4.5 Gbytes and the corresponding runtime from 1.5 to 65 mins at 3.5 Gflops on a supercomputer. In all runs a shift parameter  $\sigma = 0$  was used, ensuring resolution of the eigenspectrum in the neighbourhood of  $(\omega_r, \omega_i) = 0$ . We present results of the two cases  $q_1q_2 > 0$  and  $q_1q_2 < 0$  in order to facilitate qualitative and quantitative comparisons. The symmetry of the basic flow suggests that either stationary or complex conjugate pairs of eigenmodes are to

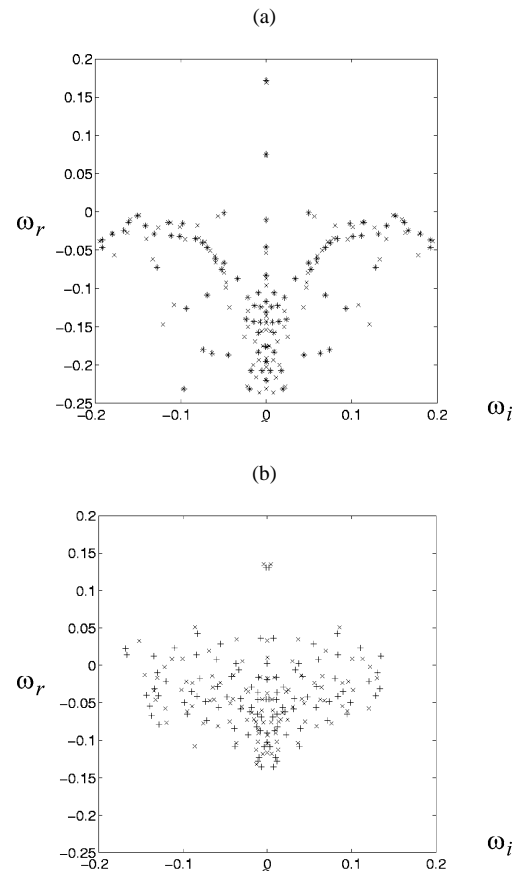


Fig. 15. Global eigenspectra at  $Re = 10^3$ ,  $k = 2/3$ : (a)  $q_2 > 0$  (co-rotating), (b)  $q_2 < 0$  (contra-rotating). The symbols correspond to different resolutions (see text).

be found in the spectrum. Indeed, this result can be seen in Fig. 15 in which the parts of the eigenspectra recovered at the two highest resolutions utilised,  $56^2$  and  $64^2$  are presented. Interesting observations are the following. First, at these parameters the biglobal instability of the flow  $q_1q_2 > 0$  can be resolved more easily in comparison with that in which  $q_1q_2 < 0$ . The lower resolution suffices to deliver several converged eigenvalues in the first case, while the higher resolution appears sufficient only for qualitative statements to be made in the second case. In both cases the most unstable mode is a stationary disturbance, i.e.  $\omega_r = 0$ . The spatial structure of which may be found in Fig. 16 through eigenfunctions  $\hat{p}(y, z)$ .

The key statement here is that the destabilisation of the model wake-vortex system can be adequately described by numerical means, using biglobal linear theory. Depending on the relative sign of the swirl parameters of the outer and inner pairs of vortices in the example presented *either vortex pair system may be destabilised* and eventually lose its coherence on account of the linear mechanism discussed. In both occasions the periodicity length of instability,  $L_x$  is comparable with the spacing of the outer vortices, and is an order of magnitude smaller than that of Crow instability. Results of comparisons with earlier works have been obtained

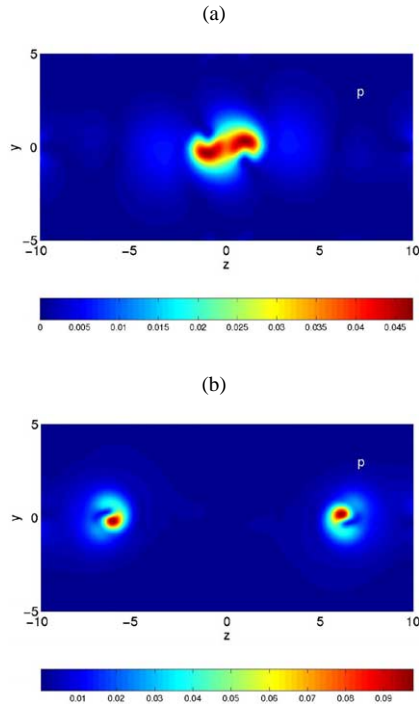


Fig. 16. Spatial structure of the most unstable global eigenmodes:  $|\hat{p}(y, z)|$ : (a)  $q_2 > 0$  (co-rotating), (b)  $q_2 < 0$  (contra-rotating).

and presented by Hein and Theofilis [21]. Here it suffices to stress that global instability theory based on numerical solution of (24) emerges as one viable alternative to assist the current efforts to minimise the coherence of the wake-vortex system, which delivers results of the quality of direct numerical simulations at a negligible fraction of the cost of the latter approach, while retaining the generality that is necessary to address realistic aircraft wake configurations.

#### 4. Experimental characterizations of unsteadiness

In this section we come back to experimental results and focus on the unsteady properties of aircraft wakes. The results are then discussed in the light of theoretical results.

##### 4.1. LDV measurements

It is usually found that the energy of the velocity perturbations within a vortex reaches its maximum in the vortex centre. Fig. 17 shows the variation with the downstream distance of the peak turbulence rate  $\sqrt{k}/V_\infty$  measured with a 3D-LDV system in the centre of the wing tip vortex of the A300 model presented in Section 2. It is observed that the turbulent kinetic energy  $k$  first decays and then remains almost constant beyond 3 spans. In the high lift case, the merger takes place at  $x/b \approx 2$ . The damping of the energy decrease beyond this distance shows existence of a mechanism that produces perturbations. If not,  $\sqrt{k}/V_\infty$  would decrease monotonously under diffusion and dissipation. This

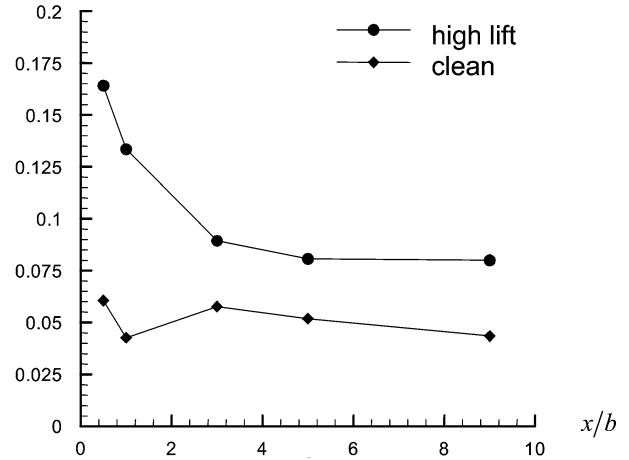


Fig. 17. Downstream evolution of the peak value of the turbulence rate  $\sqrt{k}/V_\infty$  measured with a 3D-LDV system in the centre of the wing tip vortex of a A300 model in the high lift and clean configurations (in the high lift case, merging with the flap vortex occurs around  $x/b = 2$ ; from [24]).

production could come from the development of long-wave and short wave cooperative instabilities.

##### 4.2. Hot wire measurements

The perturbations characterised above do not correspond to an equilibrium turbulence but are characteristic of a global “meandering” of the vortices. This effect is clearly evidenced by considering the spectral contents of the perturbations. Fig. 18 shows the energy density of the axial component of the velocity measured using a standard single wire Disa P11 probe placed in the centre of the high lift and clean configuration vortices at  $x/b = 5$ . Some characteristic slopes are indicated. It is seen that the vortex meandering corresponds to a broadband spectrum which exhibits a sharp energy excess for frequencies smaller than, let’s say  $f \leq 1000$  Hz (red curves). Searching for possible relationships with instabilities leads to identification of energy overshoots in the spectra. In the high lift wake vortex system, three energy accumulations may be identified (see arrows in Fig. 18). They are located at, approximately,  $f \approx 15$  Hz, 55 Hz and 400 Hz. These energy peaks are not found in the clean case shown in Fig. 18(b), except an energy bump around the first of these frequencies. It is also very clear from these figures that the small scales of the clean case vortex are much less energetic than in the high lift case.

Thus, one may wonder if these features are related to linear mechanisms. Some answers were proposed by Jacquin et al. [24]. They are summed-up below with some additional remarks that can be made in the light of the new theoretical results presented in Fig. 13 concerning short-wave instabilities.

– As seen in Section 3.2, the theoretical wavelength for the Crow instability which may develop in a dipole or in a four-vortex arrangement is  $k\tilde{b} \approx 0.8$  which means  $\lambda_{\text{Crow}} \approx 8\tilde{b}$ . At  $x/\tilde{b} = 5$ , one has  $\tilde{b} \approx 340$  mm which gives  $f_{\text{Crow}} =$

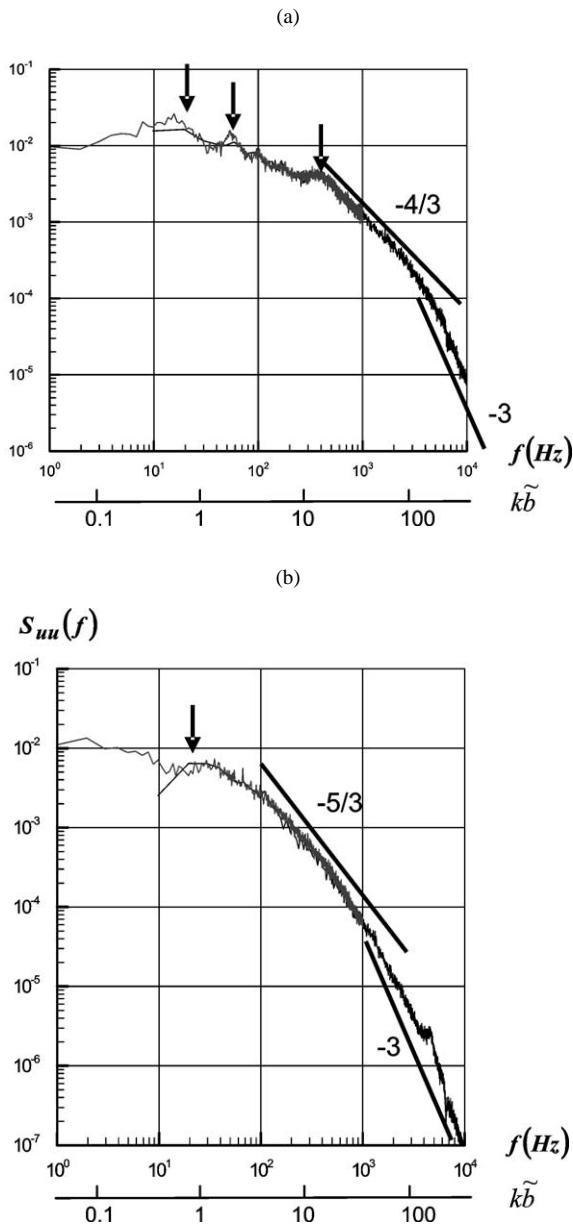


Fig. 18. Spectral densities of the axial component of velocity measured with a hot-wire probe in the center of the vortex at  $x/b = 5$ . (a) High lift case, (b) clean case. The grey and black curves correspond to 20 kHz and 2 kHz sampling, respectively. Arrows indicate the location of energy peaks (from [24]).

$V_\infty/\lambda_{\text{Crow}} \approx 18$  Hz, a value close to 15 Hz. Consequently, the peak located around  $f \approx 15$  Hz may correspond to the emergence of a long-wave cooperative instability of this type. The “signature” of a four vortex instability was detected in two-point correlations measured in the high lift case, see [24]. Such a four vortex instability could contribute to differences in the low frequency energy in Figs. 18(a) and 18(b).

– The amplification rate of the Crow instability is  $\sigma_{\text{Crow}} \approx 0.8\Gamma/(2\pi\tilde{b}^2)$ . As seen in Section 3.2, it may reach a value ten times higher when co-operation with an inner counter-rotating vortex pair is accounted for. Development of such

long-wave instabilities takes place on a characteristic distance  $x = V_\infty/\sigma$ . Using an elliptic model for evaluating  $\Gamma$  and  $\tilde{b}$  (see Section 2), the characteristic distances corresponding to an  $e^1$  amplification of the Crow instability is found to be  $x/b \approx 30$  in the high lift case ( $C_L \approx 1.7$ ) and  $x/b \approx 70$  in the clean case ( $C_L \approx 0.7$ ). These distances become ten times smaller if a four vortex system is considered. In conclusion, only the very first stages of the development of the Crow instability can be felt at  $x/b = 5$ . But the vortices are very concentrated and slight vortex displacements may generate strong fluctuations on a fixed hot wire probe. So, the first energy peak observed in the spectrum in Fig. 18 may possibly be attributed to the early stages of a long-wave cooperative instability.

– The short-wave instabilities are considered now. In the clean case, we saw that a Betz-like vortex with  $\alpha \approx 0.55$  fits correctly the velocity profile of the clean case vortex at  $x/b = 5$ , see Fig. 3(b). In this case, from Fig. 13 it is found that the first short-wave cooperative instability occurs around  $k_c\tilde{b} \approx 95$  that is  $f_c \approx 2200$  Hz using  $\tilde{b} = 340$  mm. In Fig. 18(b), such high frequencies correspond to very low levels of energy compared with those of the low frequency part. The conclusion is that, as suggested by theory, short wave instability contributions are almost undetectable in the clean case.

– Things are different in the high lift case. First, the presence of a plateau region shown in Fig. 2 leaves room for occurrence of short-wave instabilities at smaller frequencies than in the clean case, as suggested by Fig. 13. The third energy peak found at  $f = 400$  Hz in Fig. 18(a) corresponds to a wavelength  $\lambda \approx 0.125$  m, giving  $k\tilde{b} \approx 17$ , which is not incompatible with the tendencies depicted by the plateau model in Fig. 13. The much higher energy contained in these intermediate frequencies in Fig. 18(a) compared with Fig. 18(b) does suggest that short wave instabilities could be more active there. This effect is also illustrated in Fig. 19 which shows the product  $f \times S_{uu}(f)$  obtained when the hot wire is moved along a vertical line crossing the vortex core up to its centre. Each curve corresponds to a displacement of  $\Delta z = 1$  mm. Integral under these curves corresponds to the signal energy. It is seen that energy of the perturbations undergoes a dramatic increase within a distance of 1–2 mm when approaching the vortex axis. The energy increase essentially comes from short-wave contributions.

– Note finally that neutral Kelvin waves, initiated by perturbations emanating from the model (turbulence, separations, etc.) and propagating downstream along the vortex, see Section 3.1, may also contribute to the broadband spectra shown in both Figs. 18(a) and (b). Viscous instabilities of the kind considered by Fabre and Jacquin [17] and presented in Section 3.4 may also be present.

#### 4.3. PIV measurements

PIV measurements enable us to characterise vortex unsteadiness in a different way. One considers here the wake

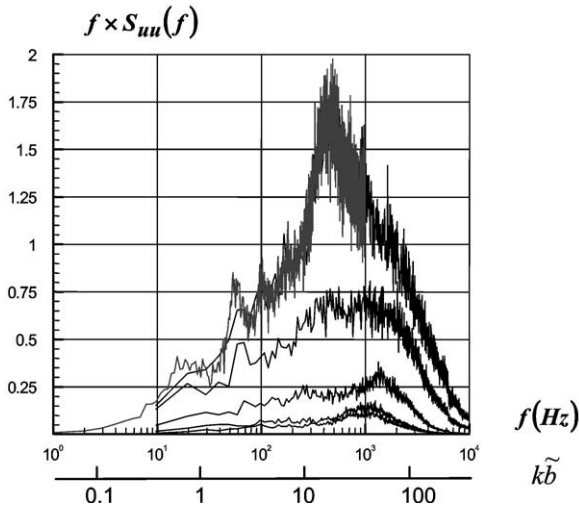


Fig. 19. Lin-log plot of  $f \times S_{uu}(f)$  obtained by translation of the hot wire in the vortex of the high lift case at  $x/b = 5$ , along a vertical line crossing the vortex core. The grey and black curves correspond to 20 kHz and 2 kHz sampling, respectively. The highest energy is obtained on the vortex axis. Each curve corresponds to a displacement of  $\Delta z = 1$  mm with respect to the vortex axis.

generated by a 1:13.6 A320 half-model with a semi-span equal to 1.25 m. The experiment was conducted in DNW-LLF. For three different configurations of the wing, samples of one to two hundred particle images were taken and the vector fields evaluated. Besides some exceptions which showed three vortices, the topology of the field in the frame of reference of the camera was formed by two vortices in each half plane, as shown in Fig. 20. In order to estimate the position and strength of the vortices, the velocity field was approximated by two Lamb–Oseen vortices. The distributions of circulation  $\Gamma$  and radius  $a$ , cf. Eq. (5), were investigated. The mean value and the standard deviation of both quantities are given in Table 1. Though this overlay of velocity fields is not consistent with Navier–Stokes equations the approximation is acceptable as shown in Fig. 20(b), see also [51]. In Fig. 21, variation of the vortex centre points for three different model configurations have been plotted. Both the vortex displacements depicted in Fig. 21 and the variations in the model parameters in Table 1 define measures of the unsteadiness of the vortices.

Fig. 21 gives an indication about meandering amplitude whose typical value is found to be  $\delta \approx 0.05$  m, that is  $\delta/b \approx 0.02$ . This value is much higher than those which were inferred from LDV measurements in the experiment presented above. It is seen that the flap vortex is subjected to larger excursions than the wing tip and that its movements admit a preferential orientation which suggests a cooperative instability. This result could confirm that multi-polar wakes are much more unstable than dipolar ones. From Fig. 21, it can be also inferred that the “blue” and “green” model planforms produce more unsteady wakes than the “red” one. At last, the fluctuations of circulation and vortex core radius

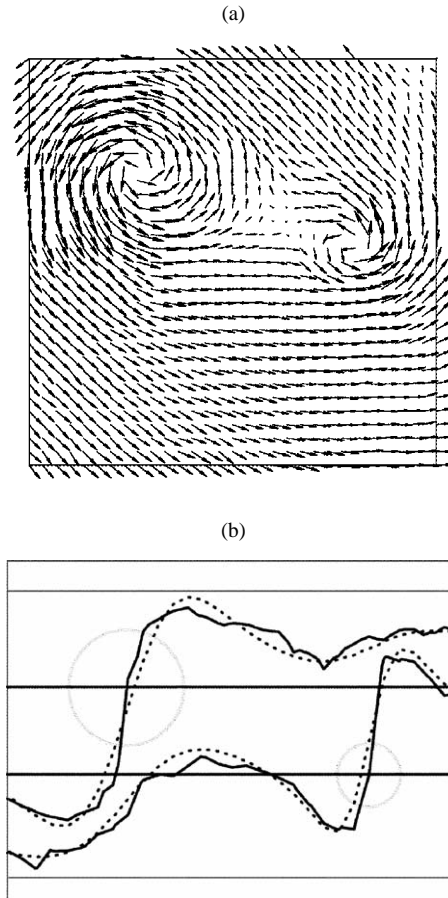


Fig. 20. (a) The velocity field with two vortices generated by flap and tip of a model wing is approximated by superposing the velocity fields of two Lamb–Oseen vortices, (b) comparison of vertical component of velocity in cuts through the approximated vortices (dashed lines) given in figure (a) PIV data in solid lines. Circles represent location and radius of Lamb–Oseen vortices.

Table 1  
Mean values and standard deviation  $\sigma$  of approximations of velocity fields by two Lamb–Oseen vortices for different configurations of a half model

	$\Gamma_1$ ( $\text{m}^2\text{s}^{-1}$ )	$\Gamma_2$ ( $\text{m}^2\text{s}^{-1}$ )	$a_1$ (m)	$a_2$ (m)
Case m06				
Mean	12.3	5.1	0.0501	0.0251
$\sigma$	0.32	0.258	0.00197	0.00245
$\sigma/\text{Mean}$	2.6%	5.1%	3.9%	9.7%
Case m04				
Mean	10.4	5.6	0.0504	0.0345
$\sigma$	1.08	0.711	0.00789	0.00869
$\sigma/\text{Mean}$	10.4%	12.7%	15.6%	25.2%
Case m05				
Mean	10.4	5.6	0.0506	0.0352
$\sigma$	1.00	1.02	0.00737	0.0136
$\sigma/\text{Mean}$	9.6%	18.1%	14.5%	38.6%

which are reported in Table 1 show that the configuration corresponding to case m05 is more unsteady than the others.

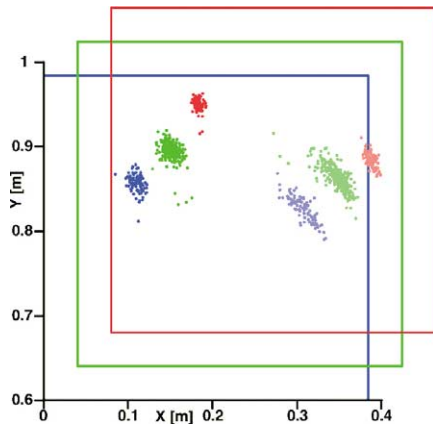


Fig. 21. Distribution of center points from the approximation by two Lamb–Oseen vortices. The different colors refer to different configurations of the same model (95 samples in blue, 298 in green, 100 in red). The different rectangles refer to the same region of the flow. The clusters on the left and right hand sides correspond respectively to the wing tip and flap tip vortices.

## 5. Conclusions

This paper aimed at presenting the status of our understanding of unsteadiness in wake vortices which has been gained both from theoretical analysis of model vortex flows and from experimental investigations of representative trailing wakes. At first, the mean flow properties of the wake have been characterised, using both a simple phenomenological model for the far-field wake, and an experimental illustration taken from the wind-tunnel experiment of Jacquin et al. [24] for the near-field wake. The main points are (i) that near-field wakes are typically composed of several vortex pairs, and (ii) that the vortex cores are poorly described by standard models such as the Lamb–Oseen vortex. A two-core scale model is recommended.

A theoretical review of basic linear mechanisms has then been presented, for generic configurations and for more realistic models. The mechanisms which have been addressed are (i) the Kelvin waves propagating along the vortex cores, (ii) the long-wave cooperative instabilities developing in wakes composed of several vortices, (iii) the short-wave cooperative instabilities (Widnall instabilities) occurring in realistic vortices subjected to a strain field, and (iv) the instabilities due to core axial flow. Specific methods used to describe these mechanisms have been presented, and a more general approach based on a global eigenvalue method has been introduced. The most interesting mechanism is the second one, which is particularly efficient in the presence of inner vortices with counter-rotating vorticity. This mechanism may be used to accelerate the dissipation of the wake.

Experimental unsteady measurements have then been presented and discussed in the light of theory. These measurements reveal that the dominant unsteady mechanism occurring in the near-field wake is a global unsteady mechanism referred to as vortex meandering, which is characterised by a broadband energy spectrum. An attempt has

been made to identify the contribution of the linear mechanisms presented above to the meandering. Hot wire measurements reveal the existence of a few peaks emerging from the broadband level in the energy spectra, which could be explained by the presence of long-wave or short-wave cooperative instabilities. Some results also indicate the existence of a four-vortex interaction. However, the wind tunnel measurements presented here are limited to the near-field wake (up to nine wing spans downstream of the aircraft). This distance is not sufficient to identify clearly these instabilities and to discriminate them from other mechanisms contributing to meandering, such as the propagation of Kelvin waves. In order to observe the development of instabilities at farther distances, other experimental facilities have to be employed, such as a catapult or a towing tank.

## Acknowledgements

The authors gratefully acknowledge the European Community, the French-Service des Programmes Aéronautiques (SPAÉ) and the ONERA Federated Research Project “Wake Vortex Dynamics” for their support. The third author was partly supported by a Ramón y Cajal Research Fellowship of the Spanish Ministry of Science and Technology.

## References

- [1] R.L. Ash, M.R. Khorrami, Vortex stability, in: S.I. Green (Ed.), *Fluid Vortices*, Kluwer, 1995.
- [2] A. Betz, Verhalten von Wirbelsystemen, *Z. Ang. Math. Mech.* 12 (1932) 164–174.
- [3] Barkley, R. Henderson, Three-dimensional floquet stability analysis of the wake of a circular cylinder, *J. Fluid Mech.* 322 (1996) 215–241.
- [4] S.C. Crow, Stability theory for a pair of trailing vortices, *AIAA J.* 8 (12) (1970) 2172–2179.
- [5] J.D. Crouch, Instability and transient growth for two trailing vortex pairs, *J. Fluid Mech.* 350 (1997) 311–330.
- [6] W.J. Devenport, M.C. Rife, S.I. Liaps, G.J. Follin, The structure and development of a wing tip vortex, *J. Fluid Mech.* 312 (1996) 67–106.
- [7] L. Dieterle, K. Ehrenfried, R. Stuff, G. Schneider, P. Coton, J.-C. Monnier, J.-F. Lozier, Quantitative flow field measurements in a catapult facility using particle image velocimetry, in: *ICIASF Congress*, Toulouse, France, 1999.
- [8] C.P. Donaldson, A.J. Bilanin, Vortex wakes of conventional aircraft, *AGARDograph* 204, 1975.
- [9] C. Eloy, *Instabilité multipolaire de tourbillons*, PhD Université d’Aix-Marseille, 2000.
- [10] C. Eloy, S. Le Dizes, Three dimensional instability of Burgers and Lamb–Oseen vortices in a strain field, *J. Fluid Mech.* 378 (1999) 145–166.
- [11] C. Eloy, S. Le Dizes, Stability of the Rankine vortex in a multipolar strain field, *Phys. Fluids* 13 (3) (2001) 660–676.
- [12] D. Fabre, *Instabilités et instationnarités dans les tourbillons. Application aux sillages d’avions*, PhD Thesis, Université Paris 6, 2002.
- [13] D. Fabre, C. Cossu, L. Jacquin, Spatio-temporal development of the long and short-wave vortex pair instabilities, *Phys. Fluids* 12 (5) (2000) 1247–1250.
- [14] D. Fabre, L. Jacquin, Stability of a four-vortex aircraft wake model, *Phys. Fluids* 12 (10) (2000) 4238–4243.

- [15] D. Fabre, L. Jacquin, A. Loof, Optimal perturbations in a four-vortex aircraft wake in counter-rotating configuration, *J. Fluid Mech.* 451 (2002) 319–328.
- [16] D. Fabre, L. Jacquin, Short-wave cooperative instabilities in representative aircraft vortices, *Phys. Fluids* (2003), submitted for publication.
- [17] D. Fabre, L. Jacquin, Viscous instabilities in trailing vortices at large swirl numbers, *J. Fluid Mech.* (2003), in press.
- [18] D. Fabre, D. Sipp, L. Jacquin, Linear dynamics of a columnar vortex, In preparation.
- [19] T. Gerz, F. Holzäpfel, D. Darracq, Aircraft wake vortices – a position paper, 2001, <http://aton.cerfacs.fr/~wakenet/news/Position-paper/position-paper.pdf>.
- [20] P. Hall, N.J. Horseman, The linear inviscid secondary instability of longitudinal vortex structures in boundary layers, *J. Fluid Mech.* 232 (1991) 357–375.
- [21] S. Hein, V. Theofilis, On instability characteristics of isolated vortices and models of trailing-vortex systems, *Computers and Fluids* (2004), in press.
- [22] Th. Herbert, Secondary instability of plane channel flow to subharmonic 3D-disturbances, *Phys. Fluids* 26 (1983) 871–874.
- [23] L.N. Howard, A.S. Gupta, On the hydrodynamic and hydromagnetic stability of swirling flows, *J. Fluid Mech.* 14 (1962) 463–476.
- [24] L. Jacquin, D. Fabre, P. Geffroy, E. Coustols, The properties of a transport aircraft wake in the extended near field, AIAA paper 2001-1038.
- [25] L. Jacquin, C. Pantano, On the persistence of trailing vortices, *J. Fluid Mech.* 471 (2002) 159–168.
- [26] J. Jimenez, Stability of a pair of co-rotating vortices, *Phys. Fluids* 18 (11) (1975) 1580–1581.
- [27] M. Khorrami, On the viscous modes of instability of a trailing vortex, *J. Fluid Mech.* 225 (1991) 197–212.
- [28] S. Le Dizès, F. Laporte, Theoretical predictions for the elliptic instabilities in a two-vortex flow, *J. Fluid Mech.* 471 (2002) 169–201.
- [29] S.N. Leibovich, S.N. Brown, Y. Patel, Short waves on inviscid columnar vortices, *J. Fluid Mech.* 173 (1986) 595–624.
- [30] K. Leibovich, S.N. Stewartson, A sufficient condition for the instability of columnar vortices, *J. Fluid Mech.* 126 (1983) 335–356.
- [31] M. Lessen, P.J. Singh, F. Paillet, The stability of a trailing line vortex. Part 1. Inviscid theory, *J. Fluid Mech.* 63 (4) (1974) 753–763.
- [32] R.-S. Lin, M.R. Malik, On the stability of attachment-line boundary layers, Part 1. The incompressible swept Hiemenz flow, *J. Fluid Mech.* 311 (1996) 239–255.
- [33] E.W. Mayer, K.G. Powell, Viscous and inviscid instabilities of a trailing vortex, *J. Fluid Mech.* 245 (1992) 91–114.
- [34] D.W. Moore, P.G. Saffman, Motion of a vortex filament with axial flow, *Proc. Roy. Soc. London Ser. (A)* 272 (1972) 403–429.
- [35] D.W. Moore, P.G. Saffman, The instability of a straight vortex filament in a strain field, *Proc. Roy. Soc. London Ser. (A)* 346 (1975) 413–425.
- [36] J. Ortega, R.L. Bristol, O. Savas, Experimental study of the instability of unequal strength counter-rotating vortex pairs, *J. Fluid Mech.* 474 (2003) 35–84.
- [37] S.C. Rennich, S.K. Lele, A method for accelerating the destruction of aircraft wake vortices, *J. Aircraft* 36 (1999) 398–407.
- [38] M. Rossi, Of vortices and vortical layers: an overview, in: Maurel, Petjeans (Eds.), *Vortex Structure and Dynamics*, in: *Lecture Notes in Physics*, Vol. 555, Springer, 2000, pp. 40–123.
- [39] P.G. Saffman, *Vortex Dynamics*, in: *Cambridge Monographs on Mechanics and Applied Mathematics*, Cambridge University Press, 1992.
- [40] D. Sipp, *Instabilités dans les écoulements tourbillonnaires*, PhD, Ecole Polytechnique, Palaiseau, 1999.
- [41] D. Sipp, Weakly nonlinear saturation of shortwave instabilities in a strained Lamb–Oseen vortex, *Phys. Fluids* 12 (7) (2000) 1715–1729.
- [42] D. Sipp, L. Jacquin, Widnall instabilities in vortex pairs, *Phys. Fluids* 15 (7) (2003) 1861–1874.
- [43] P. Spalart, Airplane trailing vortices, *Ann. Rev. Fluid Mech.* 30 (1998) 107–138.
- [44] T. Tatsumi, T. Yoshimura, Stability of the laminar flow in a rectangular duct, *J. Fluid Mech.* 212 (1990) 437–449.
- [45] V. Theofilis, Globally unstable basic flows in open cavities, AIAA Paper 2000-1965.
- [46] V. Theofilis, Linear instability in two spatial dimensions, in: K. Papailiou, et al. (Eds.), *Proc. of the European Computational Fluid Dynamics, Conference ECCOMAS '98*, Athens, Greece, 1998, pp. 547–552.
- [47] V. Theofilis, Advances in global linear instability of nonparallel and three-dimensional flows, *Progress in Aerospace Sciences* 39 (4), 249–315.
- [48] V. Theofilis, S. Hein, U.Ch. Dallmann, On the origins of unsteadiness and three-dimensionality in a laminar separation bubble, *Phil. Trans. Roy. Soc. London (A)* 358 (2000) 3229–3246.
- [49] V. Theofilis, A. Fedorov, D. Obrist, U.Ch. Dallmann, The extended Görtler–Hämmerlin model for linear instability of three-dimensional incompressible swept attachment-line boundary layer flow, *J. Fluid Mech.* 487 (2003) 271–313.
- [50] C.Y. Tsai, S.E. Widnall, The instability of short waves on a straight vortex filament in a weak externally imposed strain field, *J. Fluid Mech.* 73 (1976) 721–733.
- [51] H. Vollmers, Detection of vortices and quantitative evaluation of their main parameters from experimental velocity data, *Meas. Sci. Technol.* 12 (2001) 1–9.
- [52] S.E. Widnall, D. Bliss, A. Zalay, Theoretical and experimental study of the stability of a vortex pair, in: *Aircraft Wake Turbulence and its Detection*, Plenum Press, 1971.